Assessment of local hydraulic properties from electrical resistivity tomography monitoring of a three-dimensional synthetic tracer test experiment

M. Camporese,[1] G. Cassiani,[2] R. Deiana,[2] and P. Salandin[1]

Received 8 February 2011; revised 2 November 2011; accepted 7 November 2011; published 13 December 2011.

[1] In recent years geophysical methods have become increasingly popular for hydrological applications. Time-lapse electrical resistivity tomography (ERT) represents a potentially powerful tool for subsurface solute transport characterization since a full picture of the spatiotemporal evolution of the process can be obtained. However, the quantitative interpretation of tracer tests is difficult because of the uncertainty related to the geoelectrical inversion, the constitutive models linking geophysical and hydrological quantities, and the a priori unknown heterogeneous properties of natural formations. Here an approach based on the Lagrangian formulation of transport and the ensemble Kalman filter (EnKF) data assimilation technique is applied to assess the spatial distribution of hydraulic conductivity *K* by incorporating time-lapse cross-hole ERT data. Electrical data consist of three-dimensional cross-hole ERT images generated for a synthetic tracer test in a heterogeneous aquifer. Under the assumption that the solute spreads as a passive tracer, for high Peclet numbers the spatial moments of the evolving plume are dominated by the spatial distribution of the hydraulic conductivity. The assimilation of the electrical conductivity 4D images allows updating of the hydrological state as well as the spatial distribution of *K*. Thus, delineation of the tracer plume and estimation of the local aquifer heterogeneity can be achieved at the same time by means of this interpretation of time-lapse electrical images from tracer tests. We assess the impact on the performance of the hydrological inversion of (i) the uncertainty inherently affecting ERT inversions in terms of tracer concentration and (ii) the choice of the prior statistics of *K*. Our findings show that realistic ERT images can be integrated into a hydrological model even within an uncoupled inverse modeling framework. The reconstruction of the hydraulic conductivity spatial distribution is satisfactory in the portion of the domain directly covered by the passage of the tracer. Aside from the issues commonly affecting inverse models, the proposed approach is subject to the problem of the filter inbreeding and the retrieval performance is sensitive to the choice of *K* prior geostatistical parameters.

Citation: Camporese, M., G. Cassiani, R. Deiana, and P. Salandin (2011), Assessment of local hydraulic properties from electrical resistivity tomography monitoring of a three-dimensional synthetic tracer test experiment, *Water Resour. Res.*, *47*, W12508, doi:10.1029/2011WR010528.

1. Introduction

[2] Detailed knowledge of soil hydraulic properties is essential in all hydrogeological applications requiring predictive modeling and especially for prediction of water flow and contaminant transport in heterogeneous aquifers. The challenges posed by aquifer heterogeneity are widely recognized, with abundant literature over the past decades and many research groups active in developing rigorous stochastic theories [e.g., *Dagan*, 1989; *Gelhar*, 1993; *Zhang*, 2002; *Rubin*, 2003]. Unfortunately, these theories have still not been applied extensively, due to difficulties in collecting field data suitable to characterize heterogeneity; only a handful of applications based on actual field sites have been reported [e.g., *Sudicky*, 1986; *LeBlanc et al.*, 1991; *Neuman et al.*, 2007; *Sudicky et al.*, 2010], where an exceedingly large number of sampling points was available.

[3] Many of the in situ sampling methods that can be used to determine hydrological properties are expensive and time consuming, and typically provide only point or integral measurements, which may not be suitable for characterizing heterogeneous systems. A competitive alternative is represented by geophysical methods, such as ground penetrating radar (GPR) [e.g., *Annan*, 2005] and electrical resistivity tomography (ERT) [e.g., *Binley and Kemna*, 2005], which are increasingly used in hydrological and environmental research and applications. These methods are relatively inexpensive, nondestructive, and minimally intrusive, and may allow for hydrogeological properties to

[1]Dipartimento di Ingegneria Idraulica, Marittima, Ambientale e Geotecnica, Università degli Studi di Padova, Padova, Italy.
[2]Dipartimento di Geoscienze, Università degli Studi di Padova, Padova, Italy.

0043-1397/11/2011WR010528

be estimated at scales of interest to hydrological modeling [*Rubin and Hubbard*, 2005; *Vereecken et al.*, 2006]. However, although these methods promise a significant benefit to subsurface research, they are intrinsically inaccurate, due to their need for a geophysical inversion, which is an ill-posed problem. In other words, identification of many parameters using relatively little, somewhat noisy information that is collected only at the domain boundary clearly represents a difficult challenge [e.g., *Menke*, 1984]. In addition, suitable constitutive models linking geophysical and hydrological parameters are needed [e.g., *Brovelli and Cassiani*, 2010, 2011], often to be calibrated on a site-by-site basis. These limitations can make geophysical methods more of a qualitative tool, unless information concerning the relevant hydrological processes involved are properly taken into account.

[4] A promising means of using geophysical methods effectively for hydrological characterization involves therefore acquiring time-lapse geophysical data as changes occur in an aquifer as a result of dynamical variations in the hydrological state of the subsurface. In ERT, for instance, the electrical conductivity field is reconstructed based on current and voltage measurements from boreholes and/or the ground surface. Electrical conductivity and thus voltage measurements are sensitive to changes in water saturation or solute concentration [*Archie*, 1942; *Daily et al.*, 1992]. Therefore, ERT measurements are not directly related to the hydraulic parameters needed to predict flow and transport in variably saturated porous media. For this reason, geophysical data collected statically may provide insufficient information regarding the distribution of a particular hydrological property. In a single image both "structural" information, related to the medium properties, and "dynamic" information, related to the interactions of the solute with the porous matrix and pore fluid, are present, often mixed in an inextricable manner. However, since the temporal evolution of water content or solute concentration/salinity, which obviously depend on hydraulic properties, affect electrical conductivity, a set of time-lapse data that are sensitive to changes in these hydrological state variables is more closely linked to the distribution of hydraulic properties through the underlying hydrological process [e.g., *Binley et al.*, 2002; *Kemna et al.*, 2002; *Singha and Gorelick*, 2005; *Vanderborght et al.*, 2005; *Cassiani et al.*, 2006; *Deiana et al.*, 2007, 2008; *Monego et al.*, 2010]. Several attempts to constrain the hydrogeophysical inverse problem to reduce inversion error have recently been made using time-lapse geophysical measurements through a coupled inversion approach, where the numerical models for the geophysical and hydrological processes are linked together such that the geophysical data are inverted directly for the hydrological properties of interest. Recent applications include model parameterization obtained from one-dimensional or two-dimensional infiltration experiments in the vadose zone monitored by GPR [e.g., *Looms et al.*, 2007; *Finsterle and Kowalsky*, 2008; *Jadoon et al.*, 2008] or ERT [e.g., *Lehikoinen et al.*, 2010; *Hinnell et al.*, 2010; *Huisman et al.*, 2010; *Rings et al.*, 2010] and by ERT monitoring of tracer test experiments in shallow aquifers [e.g., *Pollock and Cirpka*, 2010; *Irving and Singha*, 2010]. The advantage of coupled inversion over separated or uncoupled inversion is that it avoids the formation of geophysical tomographic images, which are subject to artifacts caused by the regularization of the geophysical inverse problem that can significantly affect the resulting hydrological state estimates [*Ferré et al.*, 2009].

[5] Although the coupled hydrogeophysical inversion is an interesting approach that deserves to be fully explored, in most cases only a deterministic or quasi-deterministic inversion framework has been considered, which does not allow for adequate assessment of the inherent heterogenous nature of the coupled hydrogeophysical system and corresponding model parameter and prediction uncertainties. On the other hand, because of the high computational effort typically required by this type of coupled inversion, only in a few cases has a stochastic approach been considered. *Kowalsky et al.* [2005], for instance, did manage to estimate soil hydraulic parameters for a two-dimensional synthetic heterogeneous example and a three-dimensional field infiltration experiment, by means of a joint inversion of GPR and hydrological data. Other studies have been limited only to two-dimensional domains, with some expedients to reduce the dimensions of the state or parameter space, such as the integration of temporal moments of electrical potential perturbations as an alternative to the full transient time series of geoelectrical signals [*Pollock and Cirpka*, 2010] or the development of a facies-based subsurface parameterization instead of a full cell-based characterization of the hydraulic properties [*Irving and Singha*, 2010].

[6] Three-dimensional reconstruction of heterogeneous fields of hydraulic conductivity has been attempted by incorporating information from other (i.e., nongeophysical) measurements (hydraulic head, hydraulic conductivity, and solute concentration) by means of Bayesian methods integrated in groundwater flow and transport modeling frameworks. *Chen and Zhang* [2006], for instance, used the ensemble Kalman filter (EnKF) [*Evensen*, 1994, 2003] to estimate the aquifer hydraulic conductivity distribution by assimilating piezometric values in a relatively limited number of points, while *Liu et al.* [2008] used EnKF to assimilate solute concentrations and assess the distribution of flow and transport parameters in an experimental site. A different approach, the maximum a posteriori probability, was adopted by *Castagna and Bellin* [2009] to interpret the measurements derived from a synthetic hydraulic tomography experiment and to characterize the spatial variability of hydraulic conductivity in two- and three-dimensional domains.

[7] In spite of the recent popularity of fully coupled inversion approaches, their superiority over "more traditional" uncoupled methods still needs to be proven. Here a recent approach [*Crestani et al.*, 2010], developed to infer the saturated hydraulic conductivity spatial distribution by the assimilation of geophysical data, is applied using electrical conductivity measurements derived from ERT imaging of a synthetic tracer test experiment. The objective of this paper is to demonstrate the effectiveness of the proposed approach, which integrates a Lagrangian transport model and an EnKF data assimilation scheme to retrieve the heterogeneous hydraulic properties at the local scale and to reduce the uncertainty typically associated to the application of stochastic theories in subsurface hydrological modeling. A three-dimensional synthetic heterogeneous aquifer with known statistics (mean, variance, and correlation scales of

the hydraulic conductivity field) is first generated. A hypothetical tracer cloud with known initial distribution is then released and the plume evolution in response to a natural gradient is monitored by the ERT technique in a 3-D cross-borehole setting. The electrical conductivity field derived from a state-of-the-art geophysical inversion is then assimilated into the transport model by means of an ensemble Kalman filtering approach for a number of different numerical experiments. Each scenario is characterized by different values of the prior statistical parameters of the hydraulic conductivity field and different thresholds for the electrical conductivity values to assimilate, giving useful insights about the capabilities of the proposed approach to retrieve hydraulic properties of natural formations in real world applications.

2. Theory and Methods

2.1. Flow and Transport Model

[8] Following *Dagan* [1987], we consider a steady velocity field $\mathbf{V}(\mathbf{x})$ in a saturated heterogeneous porous formation where the concentration is $C = 0$ everywhere. At time $t = t_0$, a solute cloud of concentration C_0 is injected in a volume V_0. Under the assumption that the solute does not interact with the solid matrix or the pore water, the entire plume can be viewed as a sum of infinitesimal particles, each of mass

$$dM = \phi C_0(\mathbf{a}) d\mathbf{a}, \tag{1}$$

where ϕ is porosity and $\mathbf{a}$ the generic coordinate inside the volume V_0. Field findings [e.g., *Gelhar*, 1993] show that porosity in natural sedimentary formations exhibits a smaller variability than other hydraulic properties, e.g., the hydraulic conductivity $K(\mathbf{x})$, thus for the sake of simplicity ϕ is assumed constant in the whole domain. According to the Lagrangian approach, each particle moves along a trajectory of equation $\mathbf{x} = \mathbf{X}_t(t; \mathbf{a}, t_0) d\mathbf{a}$, so that the inherent associated concentration can be expressed as

$$\Delta C(\mathbf{x}, t; \mathbf{a}, t_0) = C_0(\mathbf{a}) \delta(\mathbf{x} - \mathbf{X}_t) d\mathbf{a}, \tag{2}$$

where δ is the Dirac delta function. From equation (2) the space-time definition of the concentration is straightforward and is obtained by simple integration over the whole injection volume V_0. However, our interest is related more to the average concentration $\overline{C}$ over a finite voxel ΔV whose centroid is located at $\mathbf{x}$, the resulting concentration field being

$$\begin{aligned} \overline{C}(\mathbf{x}, t; t_0) &= \frac{1}{\Delta V} \int_{\Delta V} \int_{V_0} \Delta C(\mathbf{x}', t; \mathbf{a}, t_0) d\mathbf{a} d\mathbf{x}', \\ &= \frac{1}{\Delta V} \int_{\Delta V} \int_{V_0} C_0(\mathbf{a}) \delta[\mathbf{x}' - \mathbf{X}_t(t; \mathbf{a}, t_0)] d\mathbf{a} d\mathbf{x}'. \end{aligned} \tag{3}$$

The size of the voxels can be properly chosen by taking into account also the physical device used to detect the value of $\overline{C}$ in real field applications. For instance, it may be related to the resolution of a 3-D ERT experiment, as in our case. Equation (3) links the spatiotemporal concentration distribution with the Lagrangian flow field, expressed by

$$\mathbf{X}_t(t; \mathbf{a}, t_0) = \mathbf{a} + \mathbf{X} = \mathbf{a} + \int_{t_0}^{t} \mathbf{V}[\mathbf{X}_t(t'; \mathbf{a}, t_0)] dt'. \tag{4}$$

In equation (4) $\mathbf{a}$ represents the coordinate vector at time $t = t_0$ of each trajectory within the volume V_0, whereas $\mathbf{X}$ is the displacement originating from the fluid convection process. In porous formations the effective velocity is $\mathbf{V} = \mathbf{q}/\phi$, $\mathbf{q}$ being Darcy's velocity, which can be obtained, for the case of a steady flow field, from the solution of the fluid mass balance equation:

$$\nabla \cdot \mathbf{q}(\mathbf{x}) = -\nabla \cdot [K(\mathbf{x}) \nabla h(\mathbf{x})] = 0, \tag{5}$$

subject to Dirichlet and/or Neumann boundary conditions and where h is hydraulic head.

[9] In natural aquifers $K(\mathbf{x})$ manifests spatially erratic fluctuations characterized by a correlation length λ, and dispersion of tracer solutes is dominated by the spatial variability of hydraulic properties at large scales [e.g., *Gelhar*, 1993; *Dagan*, 1989]. As a consequence we assume that all phenomena occurring at a spatial scale $\lambda << \lambda_0$ can be neglected, λ_0 being the characteristic pore scale. Under this hypothesis, the dispersion process depends only on the spatial variability of the saturated hydraulic conductivity, which controls, via (5) and (6), the tracer evolution described by (3). In this study the 3-D Lagrangian transport is simulated by means of a finite volume solver for steady state groundwater flow, coupled with the Pollock's particle tracking algorithm for the computation of particle trajectories [*Pollock*, 1988; *Salandin et al.*, 2000]. Realizations of the random function $K(\mathbf{x})$ are carried out by an improved sequential Gauss simulation algorithm [*Baú and Mayer*, 2008] similar to the one developed by *Deutsch and Journel* [1997]. The hydraulic conductivity field is assumed log-normally distributed ($Y = \ln K$) with expected value $\langle Y \rangle$, variance σ_Y^2, and exponential isotropic correlation structure $\rho_Y = \exp(-|\boldsymbol{\xi}|/\lambda)$, $\boldsymbol{\xi} = \mathbf{x_2} - \mathbf{x_1}$ being the lag distance. The flow field is then calculated by the finite volume solver at steady state with appropriate boundary conditions that ensure a mean gradient $\mathbf{J} = \text{const}$. The Eulerian velocity field is used for the computation of the trajectories of a number N_p of particles suitable for the simulation of a contaminant release. Denoting by $M = \phi C_0 V_0$ the integration of (1), i.e., the total mass uniformly injected in the system, a dimensionless concentration field is computed as [*Crestani et al.*, 2010]

$$\begin{aligned} \tilde{C}(\mathbf{x}, t; t_0) &= \frac{\phi}{M} \int_{\Delta V} \int_{V_0} C_0(\mathbf{a}) \delta[\mathbf{x}' - \mathbf{X}_t(t; \mathbf{a}, t_0)] d\mathbf{a} d\mathbf{x}' \\ &= \frac{1}{N_p \Delta V} \int_{\Delta V} \sum_{i=1}^{N_p} \delta[\mathbf{x}' - \mathbf{X}_t(t; \mathbf{a}_i, t_0)] \Delta\mathbf{a} d\mathbf{x}', \end{aligned} \tag{6}$$

where, with respect to equation (3), the continuously distributed injection in V_0 is substituted by the release of a finite set of particles regularly spaced at intervals $\Delta\mathbf{a}$, being $\Delta\mathbf{a} << \Delta V$ and $\mathbf{a}_i$ the centroid of $\Delta\mathbf{a}$.

2.2. Geophysical Model and Inversion

[10] Electrical conductivity of porous media depends mainly on moisture content, pore water salinity, and, in clay-rich formations, on the surface conductivity of the solid matrix. Neglecting the latter term, the above relationship is generally expressed by Archie's law [*Archie*, 1942]:

$$\sigma = \frac{1}{a}\ \phi^m\ S_w^n\ \sigma_w, \tag{7}$$

where σ is the bulk electrical conductivity, σ_w is the electrica conductivity of the pore water, S_w is water saturation (always equal to 1 in this study), ϕ is porosity, and a, m ("cementation exponent"), and n ("saturation exponent") are site-specific empirical parameters.

[11] Electrical resistivity tomography (ERT) allows the reconstruction of the bulk electrical conductivity field σ in 2-D or 3-D space and in time-lapse, starting from current I and voltage V measurements (and the corresponding resistance values, as voltage/current ratios) at electrodes placed at the ground surface and/or in boreholes [*Binley and Kemna*, 2005]. In order to derive the electrical conductivity images, an inversion procedure is implemented that must make use of (i) a forward model, predicting resistance values, given the space-time distribution of bulk electrical conductivity, and (ii) an inverse procedure aimed at guiding the forward model to matching the experimental data. The forward model is generally a numerical solution of the partial differential equation:

$$\nabla \cdot (\sigma \nabla V) = 0, \tag{8}$$

subjected to suitable boundary conditions. The inverse procedure seeks an electrical conductivity distribution that reproduces the data to a specified level of uncertainty, usually derived from a quantitative estimate of measurement errors. This is generally achieved by minimizing a penalty function constructed as a sum of the squared differences between measured and simulated data, weighted with the inverse of squared data errors. However, since the inherent nonuniqueness of the resistivity inverse problem can effectively lead to an ill-posed problem, additional constraints must be imposed on the inversion. This is normally accomplished by solving the inverse problem as a regularized optimization problem [*Tikhonov and Arsenin*, 1977] where the objective function to be minimized can be expressed as

$$\psi(\mathbf{m}) = \psi_d(\mathbf{m}) + \alpha\psi_m(\mathbf{m}), \tag{9}$$

with ψ_d being the data misfit:

$$\psi_d(\mathbf{m}) = ||\mathbf{W}[\mathbf{d} - \mathbf{f}(\mathbf{m})]||^2, \tag{10}$$

where $\mathbf{m}$ is the vector of unknowns distributed over a grid, and generally consisting of the log-transformed electrical conductivities of each grid voxel; $\mathbf{d}$ is the vector of data, generally consisting of the log-transformed electrical resistances measured at each quadripole of electrodes; $\mathbf{f}(\mathbf{m})$ is the vector of electrical resistances predicted by the forward model based on the numerical solution of equation (8); $\mathbf{W}$ is a data weighting matrix associated with the individual (generally uncorrelated) data errors; $\psi_m(\mathbf{m})$ is a regularizing term usually constructed on the basis of a roughness matrix $\mathbf{G}(\mathbf{m})$ that in this paper has been chosen to be a numerical approximation of the second spatial derivative of the $\mathbf{m}$ field; α is a regularization parameter that controls the tradeoff between influence of data misfit and model objective function in the inversion. The optimal value of α is generally made dependent on the error level in the data, and the corresponding solution is the smoothest compatible with the data within their error bounds (an Occam's type solution), as defined by *Binley and Kemna* [2005]. The minimization of the objective function (10) is usually conducted using iterative methods (e.g., Gauss-Newton) thus requiring the computation of a Jacobian matrix $\mathbf{A}$. Correspondingly, the covariance matrix of the estimated $\mathbf{m}$ field can be computed as

$$\mathbf{C_{mm}} = (\mathbf{A}^T\mathbf{W}^T\mathbf{W}\mathbf{A} + \alpha\mathbf{G})^{-1}, \tag{11}$$

where $\mathbf{A}$, α, and $\mathbf{G}$ are computed at the convergence $\mathbf{m}$ values. Since $\mathbf{m}$ is built by the log-transformation of σ values, the corresponding measurement error covariance matrix $\mathbf{C}_{\omega\omega}$ is computed from (12) by renormalizing each term i,j as

$$C_{\omega\omega}^{(i,j)} = \sigma_b^{(i)}\sigma_b^{(j)}C_{mm}^{(i,j)}. \tag{12}$$

In this work, for both forward and inverse solution of the electrical current flow problem, we used the 3-D ERT code *R*3 by A. Binley, Lancaster University (http://www.es.lancs.ac.uk/people/amb/Freeware/freeware.htm), which is based on a finite element forward model solution and on an Occam's approach to regularized inversion.

2.3. Dynamic Data Assimilation

[12] Whatever model is used for the description of a physical process, it will be unavoidably affected by errors and uncertainties, related to the model structure, parameter estimates, initial conditions, and boundary conditions. Data assimilation (DA) techniques have the objective to combine measurements of the system state into the model in order to obtain an optimal estimate of the system state itself. There are several DA methods available in the literature. Among these, we elected to use the ensemble Kalman filter (EnKF) [*Evensen*, 2006], which is an extension of the classic Kalman filter [*Kalman*, 1960] based on a Monte Carlo approach and specifically developed for dealing with nonlinear models and measurement operators. A possible alternative could have been the extended Kalman filter (EKF), such as the one used by *Lehikoinen et al.* [2010] in their dynamic inversion of ERT data for an infiltration experiment in the vadose zone. However, the EKF would require the computation of the Jacobian matrices for both the evolution and the observation models, resulting, in our application, in a significant and unsustainable increase of the algorithm complexity. The EnKF, instead, is particularly suitable for this study because of its ease of implementation and because it can be naturally combined with the stochastic nature of the evolution model described in section 2.1.

[13] Defined as *NMC* the ensemble size (number of realizations), we consider *NMC* state vectors consisting of the

dimensionless concentrations $\tilde{C}_i$ and saturated hydraulic log-conductivities $Y_i = \ln(K_i)$:

$$\mathbf{y}^j(t) = \{\tilde{C}_1 \dots \tilde{C}_N, Y_1 \dots Y_N\}^j, \quad j = 1, \dots, NMC, \tag{13}$$

where the state vector $\mathbf{y}^j$ has dimension $2N$, with N the number of voxels of the three-dimensional grid. The basic goal of the data assimilation procedure is to estimate these uncertain states by combining information from a physical model and from available hydrogeophysical measurements in the form of ERT images. While the true concentration distribution $\tilde{C}(\mathbf{x}, t)$ is assumed to be known by *Crestani et al.* [2010], the observation data considered in this study are realistic electrical conductivity values estimated from tracer tests monitored by time-lapse ERT.

[14] Each uncertain state vector is propagated in time by the Lagrangian transport model with the only uncertain input represented by the hydraulic conductivity field $K(\mathbf{x})$. The model, based on the mass and momentum conservation principles described in section 2.1, can be written concisely as a generic vector-valued discrete-time state equation:

$$\mathbf{y}^j(t) = F[\mathbf{y}^j(t_p), \boldsymbol{\beta}^j]; \quad t_0 \le t_p < t; \quad \mathbf{y}^j(t_0) = \mathbf{y}_0^j, \tag{14}$$

with $j = 1, \dots, NMC$. The vectors $\boldsymbol{\beta}^j$ represent the sets of saturated hydraulic conductivities (we recall here that porosity is assumed constant in space and time), while the initial condition at time $t = t_0$ is given by $\mathbf{y}_0^j$, in which only the set of hydraulic log-conductivities vary with each realization, the initial concentration field being equal for each ensemble member. The operator F basically describes how the state at a previous time t_p is related to the state at the current time t.

[15] In order to estimate the system states from hydrological measurements, it is necessary to define a transfer model operator O that describes how observed variables are related to the system states. Analogously to the state equation, this model can be concisely expressed as a vector-valued discrete-time measurement equation:

$$\mathbf{z}_i^j = O[\mathbf{y}^j, \boldsymbol{\omega}_i^j, t_i], \tag{15}$$

where $\mathbf{z}_i^j$ is the jth of NMC vectors containing electrical conductivity data obtained at time t_i and $\boldsymbol{\omega}_i^j$ is a random noise term that accounts for measurement errors. In this specific case O reflects therefore the constitutive relationship linking concentrations to electrical conductivities. More details on this relationship, which involves Archie's law, will be given later on in section 3.2.

[16] At time t_0, each state vector $\mathbf{y}^j$ associated with replicate j is initialized with the same field of initial concentration $\tilde{C}_0$ uniformly distributed over V_0, but a different realization of the hydraulic log conductivity distribution $Y(\mathbf{x})$. Analogously, each vector $\boldsymbol{\beta}^j$ contains a realization of the hydraulic conductivity distribution $K(\mathbf{x})$ used to solve the steady state flow field. For each replicate, the state vector is propagated forward in time to the first measurement time t_1, according to equation (14). Note that in the process only the concentrations vary, while the hydraulic log-conductivities remain unchanged. At t_1 each replicate, including the hydraulic log-conductivities, is updated (or conditioned) to reflect the effect of the measurements $\mathbf{z}_1$. The new vectors $\boldsymbol{\beta}^j$ are then built using the updated hydraulic conductivities and the transport problem is solved again for the time period $[t_0, t_2]$. This process continues sequentially: first a propagation step over each interval between t_o and measurement time t_{i+1} and then an update step at each measurement time t_{i+1} (Figure 1). This two-step structure is slightly different from the sequence typical of Kalman filter methods, because in this case after every update we need to restart from t_0 and the same initial concentration field, in order to ensure mass conservation throughout the simulation.

[17] The update step is expressed as [e.g., *Margulis et al.*, 2002]

$$\mathbf{y}^j(t_{i+1}|Z_{i+1}) = \mathbf{y}^j(t_{i+1}|Z_i) + \mathbf{K}_{i+1}\{\mathbf{z}_{i+1}^j - O[\mathbf{y}^j(t_{i+1}|Z_i)]\}, \tag{16}$$

where the Kalman gain $\mathbf{K}_{i+1}$ is a measure of the relative level of confidence given to the model and to the measurements. The updated states are written $\mathbf{y}^j(t_{i+1}|Z_{i+1})$ to indicate their dependence on all measurements collected through t_{i+1}. The Kalman gain is dependent on the system state covariance matrix $\mathbf{C}_{yy}$, computed by sampling the

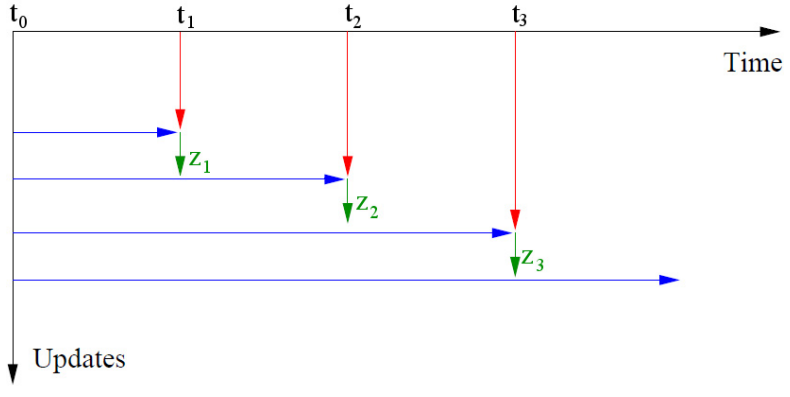

Figure 1. Illustration of the update procedure used in this study. The horizontal axis is time and the measurements are indicated at regular intervals. The vertical axis indicates the number of updates with measurements. The blue arrows represent the forward ensemble integration, the red arrows are the introduction of measurements, and the green arrows denote updates.

ensemble statistics, and the measurement error covariance matrix $\mathbf{C}_{\omega\omega}$, which is computed according to the method described in section 2.2, equation (12). The Kalman gain is expressed as

$$\mathbf{K}_{i+1} = \mathbf{C}_{yy}(t_{i+1}|Z_i)\mathbf{H}^T[\mathbf{H}\mathbf{C}_{yy}(t_{i+1}|Z_i)\mathbf{H}^T + \mathbf{C}_{\omega\omega}]^{-1}, \quad (17)$$

where the matrix $\mathbf{H}$ represents the linearization of the measurement operator O ($\mathbf{H} = O$ when the operator is linear). The computation of the update step implemented in this study follows the square root algorithm introduced by *Evensen* [2004].

3. Synthetic Tracer Test

3.1. Setup

[18] Taking L to be an arbitrary length unit, we simulate a three-dimensional aquifer with dimensions 16 L × 8 L × 8 L, discretized along each direction into $L/4$ intervals, for a total of 65 × 33 × 33 = 70785 nodes. The boundary conditions are as follows. Hydraulic head is imposed (Dirichlet) at $x = 0$ ($h = 100$ L) and at $x = 16$ L ($h = 90.4$ L), resulting in a mean gradient of 0.6 along the main flow direction, while no-flow boundary conditions (Neumann) are imposed along the remaining sides of the domain. A reference hydraulic log conductivity Y field has been generated with nominal mean $\langle Y \rangle = 0.00$ (the geometric mean saturated hydraulic conductivity $K_G = 1.0$ L/T, where T is any consistent time unit), nominal variance $\sigma_Y^2 = 0.50$ (which corresponds to a mild heterogeneity), and isotropic exponential correlation structure with integral scale $\lambda = 1$ L. The actual values of mean and variance resulting from the pseudo-random generation are $\langle Y \rangle = 0.19$ and $\sigma_Y^2 = 0.47$ (the corresponding statistics for K are $K_G = 1.21$ L/T and $\sigma_K^2 = 0.92$ L^2/T^2).

[19] The solute is assumed to be instantaneously injected in a well with diameter of 0.5 L, vertical size of 5.625 L, i.e., screened between $z = 1.375$ and $z = 7.0$ L, and centered in $x = 0.875$ L and $y = 4.125$ L. The injection is simulated by 1104 particles initially distributed along the well screen as shown in Figure 2. The dimensionless concentration $\tilde{C}$ is computed according to equation (6), i.e., proportional to the ratio between the number of particles within a voxel of the domain and the total number of injected particles. A larger number of particles would probably result in sharper concentration images and improved electrical tomograms. However, the objective here is to reproduce a realistic, albeit synthetic, experiment and we thus accept blurrier concentration images. The concentration distribution $\tilde{C}(\mathbf{x})$ is recorded every 0.5 T, for a total of 16 concentration images that are used as input for the generation of as many electrical conductivity images by the hydrogeophysical inversion procedure described in section 2.2.

3.2. Geophysical Inversion

[20] We completed the synthetic model described in section 3.1 by assuming that 12 boreholes equipped with electrodes are available for a 3-D time-lapse ERT acquisition. The boreholes are located as shown in Figure 2 defining 5 ERT blocks along the plume path. Each borehole is equipped with 16 electrodes, vertically spaced 0.5 L. Each ERT block is bounded by four boreholes, and the inner part is a squared-base rectangular prism 1.75 L wide and 7.5 L high. For the purpose of electrical forward and inverse modeling, each block is modeled separately, with a finer discretization in the region between boreholes and a progressively coarser mesh in the outer part. All boreholes are assumed to have the first electrode at $z = 8.0$ L (ground surface) and therefore the deepest electrode is at $z = 0.5$ L. The inner part of the block is discretized into 28 × 28 × 30 finite elements (rectangular parallelepipeds) having dimensions 0.0625 L × 0.0625 L × 0.25 L. In total, including the elements outside the block, each finite element mesh is composed of 48 × 48 × 44 elements. In all blocks and at all simulated measurement times, the forward model was run to produce a simulated data set composed of 1653 measurements acquired according to a completed skip-2 dipole-dipole configuration (dipole separation of three electrodes), involving all 64 electrodes located in the four boreholes bounding the block. The only error present in the simulated data is the numerical error of the finite element solution of the forward model, which has been estimated to be on the order of a few percent of the simulated resistances.

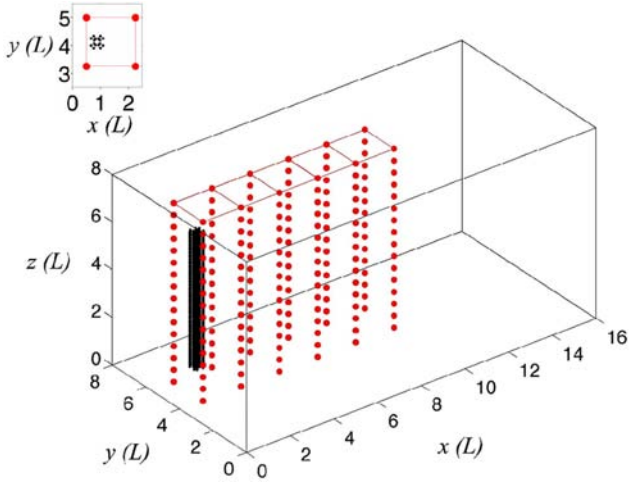

Figure 2. Schematic representation of the ERT configuration, with indication of the electrodes (red points) and the five blocks. The initial distribution of the particles (black points) along the simulated well is also shown (the upper left inset box represents a zoomed plan view).

[21] In order to compute the bulk electrical conductivity σ from the simulated dimensionless solute concentration, we applied Archie's law (8) for fully saturated media, using a porosity ϕ equal to 30%, a cementation exponent $m = 1.3$ and a parameter a equal to its theoretical value of 1. We decided not to introduce uncertainty with respect to the Archie's law parameters (the formation factor a/ϕ^m, essentially). There are some well defined reasons for this. (i) We wanted to assess the performance of the proposed approach highlighting its essential features, with no interference of other uncertainty issues. (ii) If the formation factor is assumed to be spatially homogeneous, albeit uncertain, the expected impact on the results of our analysis is minimal. Archie's law is a linear relationship for any value of a/ϕ^m under saturated conditions. Since the key information for hydraulic conductivity estimation is the tracer arrival time, and not its true concentration, an incorrect value of this concentration still contains the same key information. This has been acknowledged

recently by, e.g., *Irving and Singha* [2010], who studied the impact of Archie's law parameter uncertainty in a similar framework. (iii) If the formation factor is assumed to be spatially heterogeneous, the consequences will impact the results well beyond the scope of the present paper. In order to convert dimensionless concentrations into σ_w values, we assume that the maximum dimensionless concentration (equal to 1/92 = 0.01087) corresponds to the maximum dimensional concentration of 6 g/liter, considered to be the maximum solute concentration for which gravimetric sinking is not observed. We further assume that the dissolved solute is NaCl, and we use the relationship between molar concentration and water electrical conductivity established by *Sambuelli and Comina* [2010]. Note that any other equivalent relationship would not have produced very different results. The inverse of the same relationship was used to convert forecasted dimensionless concentrations into σ values for data assimilation (operator O in equations (15) and (16)).

[22] In order to reduce the number of degrees of freedom of the inverse problem, the ERT inversion parameterization was a $2 \times 2 \times 2$ block of neighboring finite elements ($0.125\ L \times 0.125\ L \times 0.5\ L$), sharing the same (unknown) bulk electrical conductivity value. The inversion was run independently for each block, as this approach is computationally much more efficient than inverting all collected data at once. Even though examples of inversion of a complete data set over multiple boreholes exist [e.g., *Coscia et al.*, 2011] there is no clear evidence that the results of a complete inversion are superior to splitting the inversion in blocks, as done most commonly. In our approach, anyway, we account for the presence of the plume outside the inversion block, as the 3-D finite element mesh of each block extends well beyond the four boreholes. When computing the forward model to generate synthetic data for each block we imported electrical resistivity for the entire 3-D finite element mesh, thus incorporating the effect of the plume within the entire domain. A Gaussian data error model with 5% standard deviation was assumed. Only the inner part of each block is considered to produce reliable σ estimates, so the entire plume is imaged by considering together, at each time step, the inner parts of all five ERT blocks.

3.3. Hydraulic Conductivity Estimation

[23] In order to assess the ability of the proposed approach to retrieve the reference field of hydraulic conductivity, a number of synthetic experiments were carried out. In each experiment we start from an ensemble of hydraulic conductivity realizations characterized by geostatistical properties that are intentionally different from those used to create the reference field. The prior geostatistical parameters are assigned only at the beginning of the simulation, for the generation of the initial ensemble of realizations. These realizations are then updated only on the basis of the EnKF assimilation step and the resulting geostatistical parameters (mean, variance, correlation scale) are estimated "a posteriori" as sample statistics. Table 1 summarizes the prior geostatistical properties of the initial hydraulic log conductivity fields for each experiment. Based on previous studies [*Crestani et al.*, 2010] and preliminary runs, we elected to use an ensemble size *NMC* of 2000. Larger ensemble sizes (up to 5000) result in a significant increase of the computational effort, with a limited improvement of the EnKF performance. The prior hydraulic conductivity field has been assumed isotropic in all cases ($\lambda = \lambda_x = \lambda_y = \lambda_z$). To limit the dimension of the problem and thus the computational effort, which is basically controlled by the number of measurements to be assimilated (equations (16) and (17)), two minimum thresholds on the electrical conductivity values assimilated have been considered. As a result, we present two series of seven experiments each, the first series in which we assimilate only electrical conductivity values greater than 0.0040 S/L, the second series in which the minimum threshold is reduced to 0.0021 S/L. The second threshold (0.0021 S/L) is chosen so that we assimilate all the electrical conductivity values that are greater than the minimum electrical conductivity value corresponding to a concentration $\tilde{C} > 0$. In this way we are maximizing the information derived from the geophysical inversion but at the same time neglecting "structural" data, related to the background medium properties that are constant in time and thus not relevant. The first threshold (0.0040 S/L) has a well-defined physical meaning, as can be deduced from Figure 3, which shows the standard deviation of the electrical conductivity estimates as a function of σ itself, as computed by the geophysical inversion procedure. The threshold 0.0040 S/L corresponds to a value that allows us to consider the relationship between the estimated electrical conductivity and its standard deviation as almost perfectly linear, i.e., data point deviations from the regression line are negligible above 0.0040 S/L. Using this threshold we do not consider low σ values, associated to (i) measurement points located near the ground surface, with higher coefficients of variation (i.e., relative uncertainty), represented in Figure 3 by data above the regression line; and (ii) measurement points close to the boreholes, with lower relative uncertainty and higher ERT sensitivity, but not covered by the passage of the saline tracer, represented in Figure 3 by data below the regression line. In other words, with the first threshold (0.0040 S/L) we are considering mainly the portion of the domain that is directly covered by the plume path, i.e., the center vertical

Table 1. Nominal and Prior Geostatistical Parameters Applied in the Test Cases

Test Case	$\langle Y \rangle$	σ_Y^2	λ
Reference	0.0	0.5	1.0
1. False prior variance	0.0	1.0	1.0
2. False prior mean	−1.5	0.5	1.0
3. False prior mean and variance	−1.5	1.0	1.0
4. Overestimated prior correlation length	0.0	0.5	1.5
5. Underestimated prior correlation length	0.0	0.5	0.5
6. Overestimated prior correlation length and false prior mean and variance	−1.5	1.0	1.5
7. Underestimated prior correlation length and false prior mean and variance	−1.5	1.0	0.5

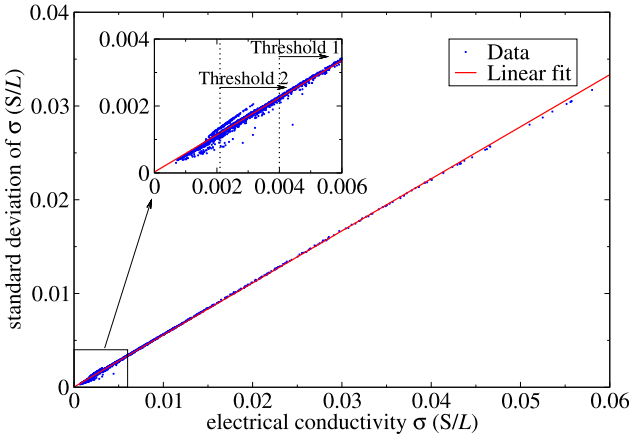

Figure 3. Synthetic ERT experiment, time 7, block 2: relationship between electrical conductivity σ and its standard deviation. Inset box represents a zoom of the zone near the origin. Points falling above the line represent nodes along the surface, where uncertainty is greater, while points falling below the line represent nodes close to the electrodes, where uncertainty is smaller.

cross section. In real field experiments, appropriate thresholds can be chosen only on the basis of information derived from the electrical tomograms available before carrying out the hydrological inversion. This is an advantage of our uncoupled inversion framework, as we have the control on the assimilation process and the option to neglect data that we consider not reliable.

[24] Note that the hydrological and the geophysical models are based on finite volume and finite element solvers, respectively, and thus work on different grids. Hence a spatial interpolation was needed to compute the relevant electrical conductivity values at the nodes of the hydrological model grid.

[25] Figures 4 and 5 show the comparison between the true synthetic hydraulic log conductivity distribution, the prior Y field for test case 1 (see Table 1), and the estimated Y field at the end of inversion in the case $\sigma_{\text{thresh}} = 0.0040$ S/L. The prior distribution of hydraulic conductivity appears homogeneous, as a result of the ensemble average of a statistically homogeneous field over 2000 realizations. From the three-dimensional cross section (Figure 4) it is not immediately apparent that a satisfactory retrieval of the Y field is achieved, especially for the portions of the

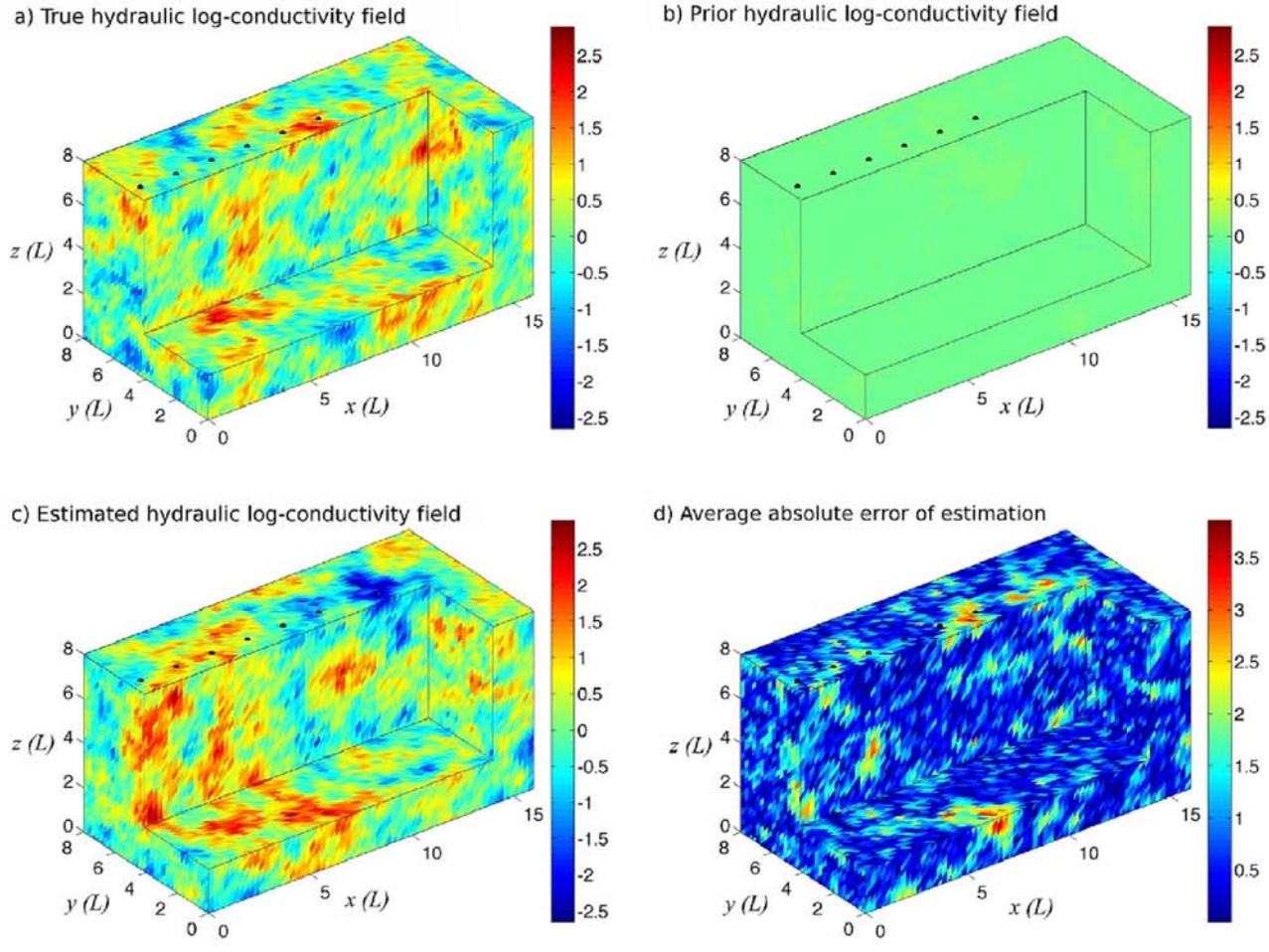

Figure 4. (a) Synthetically generated true hydraulic log conductivity field, (b) prior log conductivity field at the beginning of test case 1, (c) estimated log conductivity field resulting from the inversion in test case 1 with $\sigma_{\text{thresh}} = 0.0040$ S/L, and (d) average absolute error of estimation. Color bars indicate hydraulic log conductivity in $\ln(L/T)$ and black dots represent the only visible surface array of electrodes.

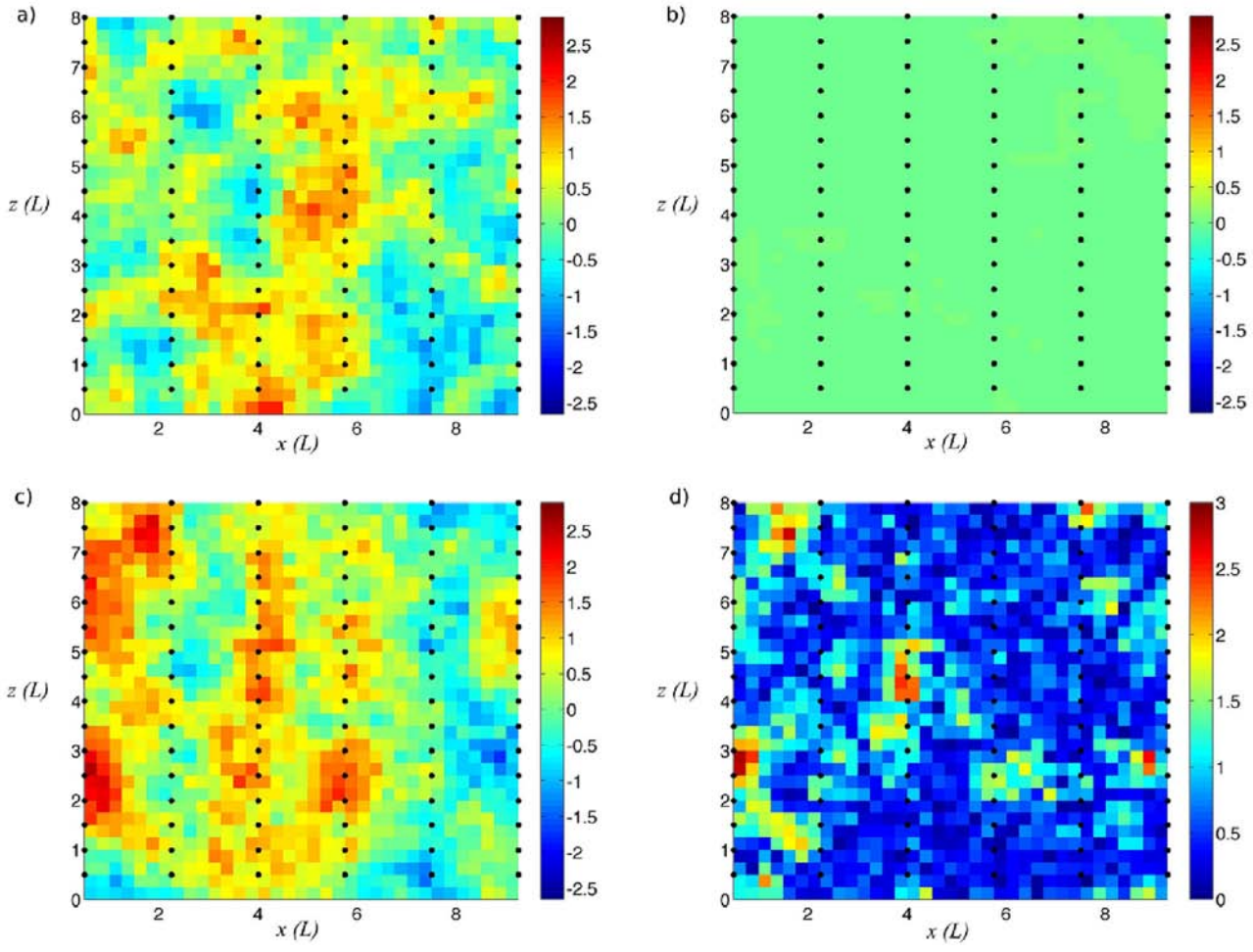

Figure 5. Same as Figure 4, but with zoomed vertical cross sections taken at $y = 4.125\ L$. (a) Synthetically generated true hydraulic log conductivity field, (b) prior field at the beginning of test case 1, (c) estimated field resulting from the inversion in test case 1 with $\sigma_{\text{thresh}} = 0.0040$ S/L, and (d) average absolute error of estimation. Color bars indicate hydraulic log conductivity in $\ln(L/T)$ and black dots represent one of the two vertical arrays of electrodes.

domain that are not "sampled" by the tracer plume, e.g., the horizontal planes at $z = 8\ L$ (for $x > 7.5\ L$) and at $z = 2\ L$ (for $y < 2\ L$). However, a closer look at a vertical cross section directly covered by the passage of the plume (Figure 5, $y = 4.125\ L$) reveals that, at the end of the inversion, some of the main features of the true aquifer are reproduced, mainly within the boreholes that form the last four ERT blocks (from $x = 2.25\ L$ to $x = 9.25\ L$). The spatial distribution of the average absolute error *AAEY*, computed as

$$AAEY(\mathbf{x}) = |\langle Y(\mathbf{x})\rangle - Y_t(\mathbf{x})|, \tag{18}$$

where $Y_t(\mathbf{x})$ is the true hydraulic log conductivity, is also shown in Figures 4d and 5d. The error spatial distribution obviously reflects the behavior of the reconstructed Y field, with values that are relatively small across most of the domain, except for a few zones of misestimation, which are clearly visible also from the comparison of panels (a) and (c). These artifacts are localized mainly outside the path of the saline tracer plume and thus are probably due to the lack of measurements (when the threshold is 0.0040 S/L) or the large uncertainty affecting the hydrogeophysical data (when the threshold is 0.0021 S/L).

[26] The fact that the retrieval of the hydraulic conductivity field is actually satisfactory is confirmed by the analysis of Figure 6, which shows the comparison at $t = 8.0\ T$ between the electrical conductivity tomogram obtained by the ERT inversion, the corresponding true tracer distribution, and the tracer distribution computed by a simulation using the Y field reconstructed in experiment 1 with $\sigma_{\text{thresh}} = 0.0040$ S/L. Using the retrieved field results in a plume pattern that has a significant effect of mass dispersion (Figure 6c). This reflects the characters typical of the electrical inversions, which are prone to overdispersion of the signal due to the regularization term (Figure 6a). Nevertheless, the shape of the plume obtained with the retrieved Y field is very similar to the true one, probably due to the fact that the assimilation process, and hence the updated distribution of hydraulic conductivity, is more sensitive to the electrical signal arrival times rather than to the actual conductivity values assimilated. We will further discuss this issue later on in section 3.3.

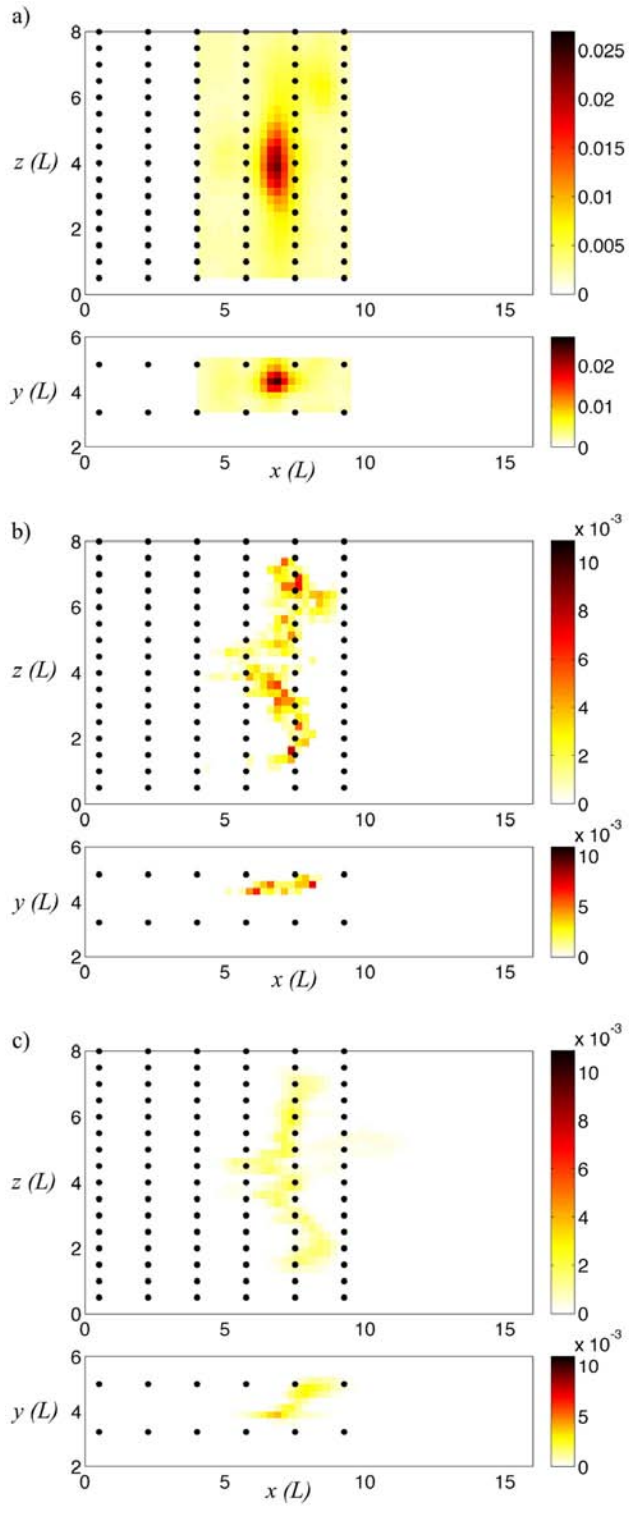

Figure 6. Comparison at $t = 8.0\ T$ between (a) the tomographic image of the electrical conductivity resulting from the electrical inversion, (b) the tracer plume simulated with the reference Y field, and (c) the tracer plume simulated with the Y field reconstructed in experiment 1 with $\sigma_{\text{thresh}} = 0.0040$ S/L. Color bars indicate (a) electrical conductivity in S/L and (b), (c) dimensionless concentration $\tilde{C}$. Black dots represent the electrodes.

[27] For brevity we do not report the visualization of the results for all the test cases; instead we summarize the inversion procedure performance in Table 2, in terms of root mean square error of the log conductivity (*YRMSE*), computed as

$$YRMSE = \sqrt{\frac{1}{N_b}\sum_{i=1}^{N_b}(\langle Y_i\rangle - Y_{t,i})^2}, \tag{19}$$

where subscript i denotes the ith node of the discretization grid and N_b is the total number of nodes falling within the ERT blocks. With this definition we do not take into account the performance of the method outside the domain defined by the ERT blocks (Figure 2). Table 2 shows also the comparison between the true and estimated hydraulic log conductivity mean and variance, computed both inside the ERT blocks and with reference to the whole domain. In general, the Y mean and variance estimated within the ERT blocks are closer to the true values than those computed for the whole domain. It is clear that the inversion procedure does not benefit by the reduction of the threshold value on the electrical conductivities to assimilate. On the contrary, the errors increase in almost all cases, even though for experiment 1 there is a slightly better estimation of the mean and variance of Y using $\sigma_{\text{thresh}} = 0.0021$ S/L. However, this could be a sheer coincidence, as an objective evaluation of the spatial field retrieval can be given only by the *YRMSE*. This behavior can be explained by comparing the true plume spatial moments with the ones computed from the ERT tomograms as a function of the threshold electrical conductivity, i.e., considering only concentration values corresponding to $\sigma > \sigma_{\text{thresh}}$. The spatial moments of the solute body are defined as follows:

$$M = \phi\int \tilde{C}d\mathbf{x}, \qquad \mathbf{R} = \frac{\phi}{M}\int \mathbf{x}\tilde{C}d\mathbf{x}$$
$$S_{ij} = \frac{\phi}{M}\int (x_i - R_i)(x_j - R_j)\tilde{C}d\mathbf{x}, \tag{20}$$

where integration is extended over the entire domain. The zero-order moment M is the total mass, $\mathbf{R}$ is the coordinate vector of the center of mass, and S_{ij}, the second-order spatial moment tensor, is proportional to the moments of inertia of the solute body. Taking into account only concentration values that correspond to electrical conductivities greater than the thresholds results in different values of the spatial moments, as shown in Figure 7. The moment components along the longitudinal direction x, which is the main direction of the plume, show that a lower threshold results in a less accurate estimate of both R_1 and S_{11}. This is due to the impact of less significant and more uncertain data that are included in the computation. Table 3, which reports the root mean square error of the inverted spatial moments with respect to the true ones, confirms this consideration: although the error on the total mass is slightly smaller for $\sigma_{\text{thresh}} = 0.0021$ S/L, the errors on the most relevant first and second moments R_1 and S_{11} are significantly smaller when using $\sigma_{\text{thresh}} = 0.0040$ S/L. A good estimate of the first and second moments can be achieved only if the mean

Table 2. Retrieval Performance of the Different Test Cases[a]

	$\sigma_{thresh} = 0.0040$ S/L					$\sigma_{thresh} = 0.0021$ S/L				
Test Case	*YRMSE*	$\langle Y\rangle_b$	σ^2_{Yb}	$\langle Y\rangle$	σ^2_Y	*YRMSE*	$\langle Y\rangle_b$	σ^2_{Yb}	$\langle Y\rangle$	σ^2_Y
Reference	–	0.23	0.46	0.19	0.47	–	0.23	0.46	0.19	0.47
1	0.93	0.44	0.52	0.44	0.70	1.11	0.45	0.81	0.18	0.67
2	1.27	−0.29	0.94	−0.84	1.14	1.35	−0.51	1.11	−0.98	1.46
3	1.27	0.01	1.02	−0.65	1.36	1.52	−0.51	1.52	−1.07	1.79
4	1.33	0.44	1.18	0.51	1.12	1.15	0.63	0.72	0.46	0.94
5	0.95	0.30	0.44	0.15	0.55	0.96	0.26	0.50	0.04	0.62
6	1.16	0.03	0.93	−0.16	1.12	1.29	−0.06	1.22	−0.62	1.41
7	1.40	−0.37	1.30	−1.10	1.46	1.82	−0.91	1.75	−1.36	1.52

[a] $\langle Y\rangle_b$ and σ^2_{Yb} are Y mean and variance, respectively, computed within the ERT blocks.

arrival times of the plume are well captured by the ERT survey. Thus, it is confirmed that for an effective assimilation of electrical data into this hydrological model it is more important to obtain a good reproduction of the tracer arrival times rather than minimize the mass dispersion effect typical of the inversion process.

[28] In general, the closer the prior statistics of Y to the true statistics, the better the overall performance of the inversion method (Table 2). However, although the minimum *YRMSE* values at the end of the inversion are achieved when the initial parameters are closer to those of the reference field, the most significant improvements are obtained when starting from a completely wrong prior Y field. This is shown in Figure 8, which depicts for all the experiments with $\sigma_{thresh} = 0.0040$ S/L the time evolution of the hydraulic log conductivity root mean square error *YRMSE* and the concentration root mean square errors *CRMSE*, the latter calculated by equation (19), using $\tilde{C}$ instead of Y. Note how in Figure 8 a wrong prior mean of Y results in a decreasing behavior of *YRMSE*, with a rapid reduction with the first updates and a stabilization toward the end of the inversion. On the other hand, when the initial root mean square error is small, *YRMSE* paradoxically increases with the updates, with a final estimation that is, on average, worse than the prior homogeneous field. This, however, does not necessarily mean that the prior homogeneous field is better at reproducing the overall transport process. The *CRMSE*, in fact, after the very first time steps during which it increases from the initial value of 0.0 (we recall that the initial position of the plume is correct throughout the experiment), constantly decreases also for the scenarios characterized by a progressive worsening of the *YRMSE*. This indicates that the reconstructed Y field, though worse on average than the prior, is able to reproduce satisfactorily the solute concentrations thanks to the main features that mimic the reference field structure. This is typical of all ill-posed inverse problems, where the optimal solution is not unique.

[29] When the first guess for the correlation lengths is wrong, but the other parameters are correct, we obtain different results depending on whether λ is overestimated or

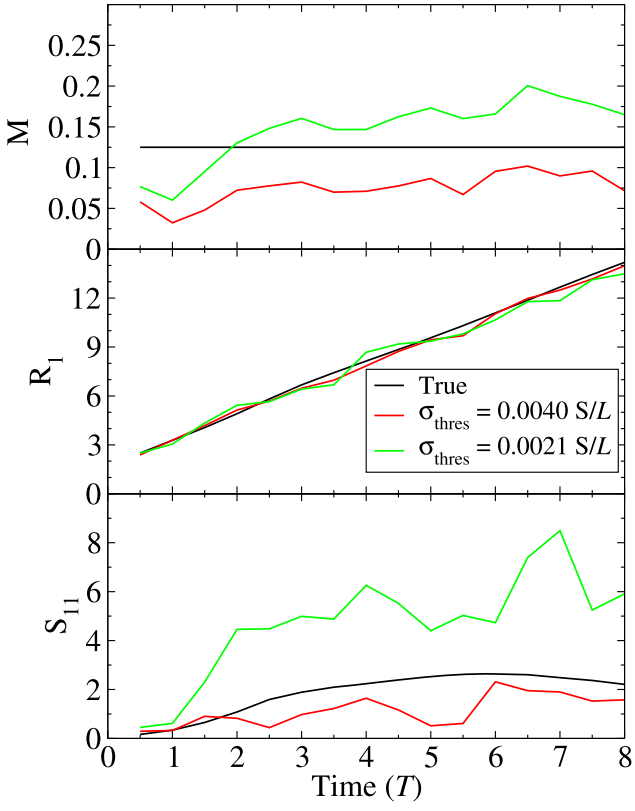

Figure 7. Time evolution of the zeroth-order spatial moment (total mass) M, the x coordinate of the first-order spatial moment (center of mass) R_1, and the x coordinate of the second-order spatial moment (moment of inertia) S_{11} for the true tracer plume and the plume reconstructed by the electrical inversions (tomographic images) with thresholds $\sigma_{thresh} = 0.0040$ S/L and $\sigma_{thresh} = 0.0021$ S/L.

Table 3. Root Mean Square Error of the Plume Spatial Moments Computed From the ERT Tomograms With Respect to the True Ones[a]

	RMSE	
Spatial Moment	$\sigma_{thresh} = 0.0040$ S/L	$\sigma_{thresh} = 0.0021$ S/L
M	0.053	0.044
R_1	0.252	0.447
R_2	0.043	0.125
R_3	0.356	0.184
S_{11}	0.967	3.170
S_{22}	0.246	0.644
S_{33}	3.828	3.270

[a] M is the zeroth-order spatial moment (total mass), R_i are the coordinates of the first-order spatial moment (center of mass), and S_{ii} are the coordinates of the second-order spatial moment (moment of inertia).

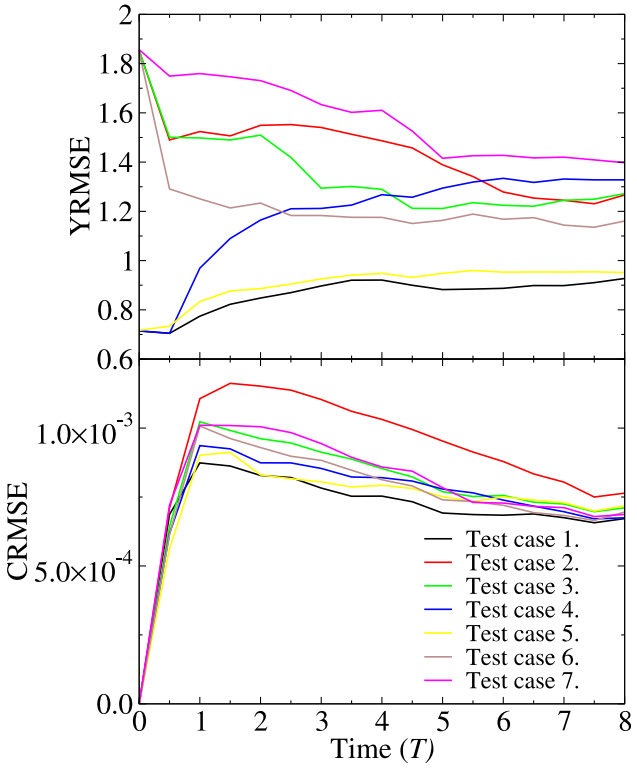

Figure 8. Time evolution of the root mean square error of the hydraulic log conductivity field (top) and concentration field (bottom) for all the experiments with $\sigma_{\text{thresh}} = 0.0040$ S/L. See Table 1 for a detailed description of all the test cases.

underestimated. We observe (Table 2) a worse performance in the former case, probably due to the uncertainty in the geoelectrical data, hence spurious updates are propagated due to a larger correlation scale. Similar results were found by *Crestani et al.* [2010]. On the other hand, the Y field resulting from the inversion with a smaller correlation length is characterized by smaller and differently shaped features with respect to those of the true Y field (not shown). At a first look, comparison between experiments 6 and 7 seems to contradict the aforementioned considerations, as in this case starting with an overestimated λ gives better results than starting with an underestimated λ. However, it must be taken into account that in experiments 6 and 7 the prior mean and variance of Y are also very different from the true values and thus a larger integral scale implies that significant corrections are propagated more rapidly. Hence, with the same number of updates, the final error in experiment 6 is smaller, as a larger portion of the domain has been corrected.

[30] In all experiments, the *YRMSE* values obtained are quite high with respect to similar studies [e.g., *Chen and Zhang*, 2006; *Crestani et al.*, 2010; *Pollock and Cirpka*, 2010]. However, this can be explained by the quality and the uncertainty of the electrical data, which are derived from a realistic ERT experiment and thus are more representative of what we can expect from a real field study, compared to a synthetic test where everything is perfectly known. It is also interesting that, contrary to *Pollock and Cirpka* [2010], in all our test cases the spatial variability of Y is overestimated. Again, this can be explained by the quality of the assimilated data, in combination with the effect of filter inbreeding (or divergence) [*Hendricks Franssen and Kinzelbach*, 2008; *Evensen*, 2009], i.e., a progressive degradation of the updates typical of the ensemble Kalman filter and caused by the loss of ensemble variance. This can be clearly seen in Figure 9, which shows the time evolution of the Y ensemble variance spatial distribution in experiment 1 with $\sigma_{\text{thresh}} = 0.0040$ S/L. The variance, which is initially spatially uniform and equal to the value imposed for the generation of the Y field, decreases sequentially at each update, following the same spatial pattern of the saline plume. As a result, the ensemble variance is drastically reduced very quickly, eventually resulting in values close to zero. According to *Evensen* [2009], we argue that spurious correlations between supposedly uncorrelated variables, caused by the finite ensemble size and the lack (or the large uncertainty) of measurements in zones of the domain not covered by the path of the saline tracer, accumulate small nonphysical updates in each ensemble member, ultimately leading to realizations that are almost equal to each other but with exaggerated hydraulic log conductivity absolute values and thus overestimated spatial variance σ_Y^2.

[31] Overestimation of σ_Y^2 implies also that the correlation structure of the true Y field cannot be easily reconstructed. Figure 10 shows the correlation structure of Y along the x direction for experiments 4 and 5 with $\sigma_{\text{thresh}} = 0.0040$ S/L. In general we observe that the initial correlation length is not easily changed by the inversion procedure; indeed the algorithm tends to maintain the correlation structure as initially hypothesized. Again, in experiment 5 the propagation of numerical artifacts is limited by the small correlation length imposed at the beginning, resulting in an estimated σ_Y^2 that is close to the true value, but only because the prior mean and variance are equal to the true values. When the prior Y field statistics are poorly known the small correlation length does not allow the corrections to be propagated (Table 2, experiment 7).

[32] Overall, the results are satisfactory, because in all the considered cases the estimated hydraulic conductivity field has been corrected in the portion of the domain directly sampled by the passage of the saline tracer and is thus suitable to reproduce a concentration distribution very similar to the reference scenario.

4. Conclusions

[33] We applied a recent hydrological inversion procedure for the assessment of heterogeneous hydraulic conductivity fields at the local scale from ERT imaging of a synthetic tracer test experiment. Using an ensemble Kalman filtering approach integrated in a groundwater Lagrangian transport modeling framework, we demonstrated that assimilation of electrical conductivity data is useful to retrieve the spatial distribution of hydraulic conductivity K. We also demonstrated how the use of electrical conductivity images derived from ERT inversion is a viable approach to hydraulic conductivity identification in tracer tests. This result is due to the fact that the data information content for hydraulic conductivity estimation is condensed in the tracer arrival times. As we consider an instantaneous injection of tracer, the relevant timing is the peak concentration arrival. Therefore,

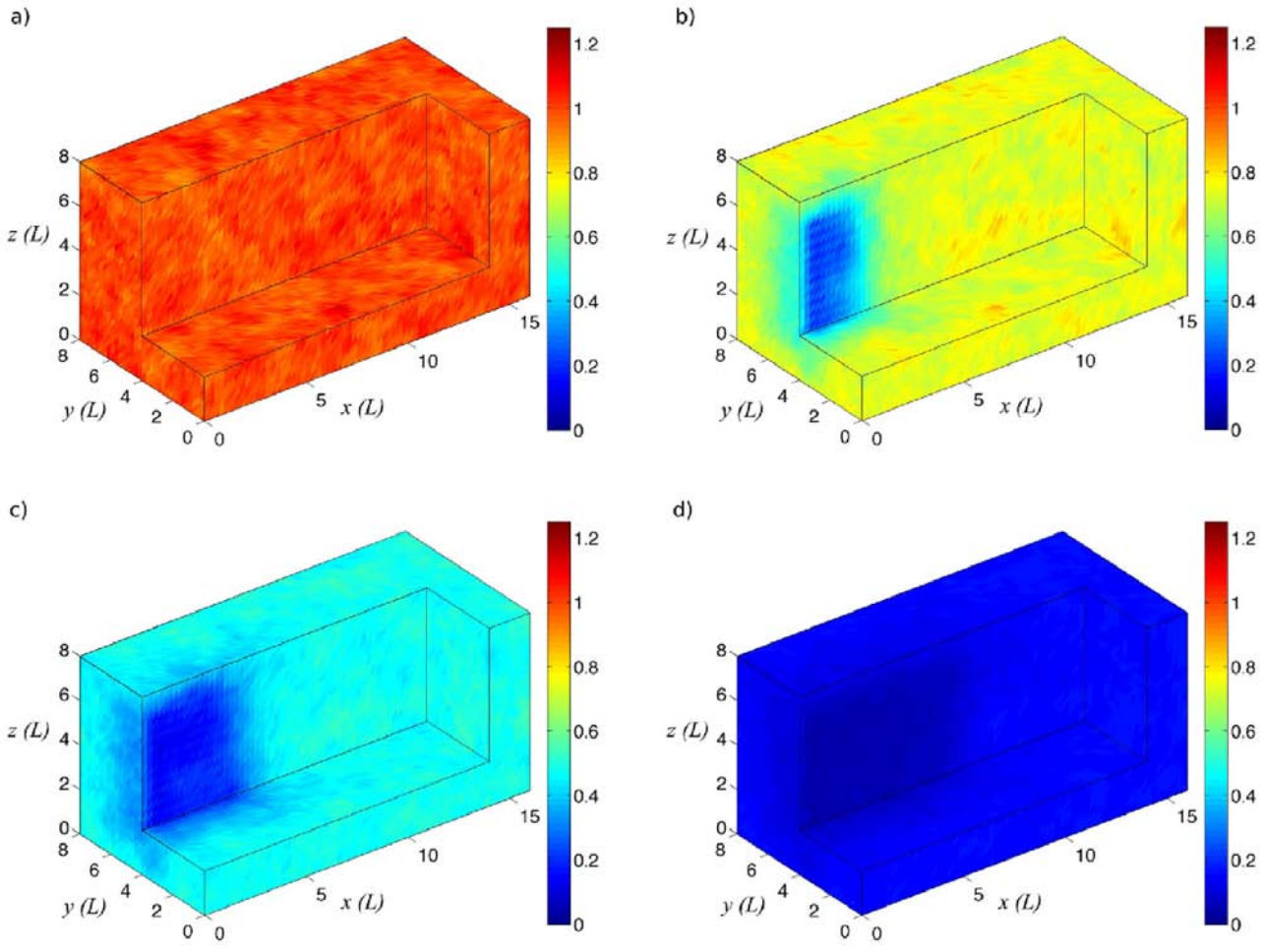

Figure 9. Spatial distribution of the ensemble Y variance at times (a) $t = 0.0\ T$, (b) $t = 2.0\ T$, (c) $t = 4.0\ T$, and (d) $t = 8.0\ T$, for experiment 1 with $\sigma_{\text{thresh}} = 0.0040$ S/L. Color bars indicate variance of hydraulic log conductivity in $\ln^2(L/T)$.

even though the absolute value of concentration may be lowered and early low concentration artifacts may be present (both caused by ERT inversion) the timing of peak arrival is unaffected, and the procedure is unbiased. In addition, our results indicate that skipping the imaging process in coupled approaches can be particularly damaging for the problem at hand, since we can only consider reliable the hydraulic conductivity distribution estimated in the region where the plume has actually traveled. The electrical resistivity images, albeit partly weakened by ERT inversion, are essential to identify the region where hydraulic conductivity can be adequately estimated.

[34] The performance of the method is affected by the quality of ERT tomograms and by the choice of prior statistics for the hydraulic conductivity field. Imposing a threshold on the electrical conductivities to be assimilated had a significant impact on the quality of the retrieved hydraulic conductivity distributions, with better performance associated to the threshold for which a better estimation of the tracer concentration spatial moments and, as a consequence, of the arrival times, was obtained. Choosing prior mean and variance of $Y = \ln K$ close to the true values resulted in a better final hydraulic conductivity distribution, but with marginal improvements with respect to the scenarios in which prior information misestimated the true statistics. The proposed algorithm is sensitive to the problem of the filter divergence, with a rapid decrease of the ensemble variance with the number of updates, associated to overestimation of the spatial variance of hydraulic log conductivity. Another important finding is that correlation lengths are difficult to correct, since the inversion procedure tends to maintain the initial values throughout the simulation. Also, overestimation of integral scale can have either positive or negative effects on the inversion, depending both on the quality of ERT data and the prior statistics used to generate the initial K field realizations.

[35] Possible directions for future studies include: the application of the proposed approach to real field experiments; the comparison with a smoothing approach, in which all time-lapse data are inverted simultaneously rather than sequentially; joint assimilation of electrical data with other types of data (e.g., piezometric values) that are often easily available in the field, although usually in a limited number of locations; the implementation of an algorithm to reduce filter inbreeding; and, most importantly, the development of an EnKF-based coupled geophysical–hydrological

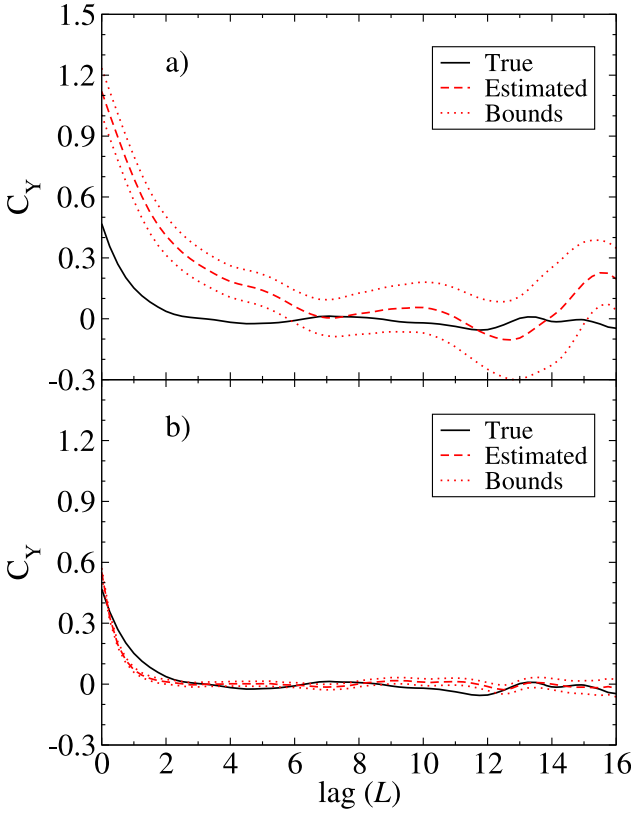

Figure 10. Comparison between the covariance structure of the reference log conductivity field and of the reconstructed fields in experiments (a) 4 and (b) 5 with $\sigma_{\text{thresh}} = 0.0040$ S/L.

inversion, which could include also the uncertainty of the petrophysical constitutive relationship, to be compared with the proposed uncoupled strategy for a better assessment of the benefits stemming from a real-time exchange of information between hydrological and geophysical processes.

[36] **Acknowledgments.** This work was supported by the Italian Ministry of University (PRIN project 200788W4EC) and by the University of Padua (projects CPDA089375 and STPD08RWBY). The authors also wish to acknowledge Andrew Binley (Lancaster University), for the use of his ERT inversion code R3, Domenico Baú (CO State University), for providing the random field generator used in this study, and the Associate Editor and three anonymous reviewers for their constructive remarks that helped to improve the quality of the paper.

References

Annan, A. P. (2005), GPR methods for hydrogeological studies, in *Hydrogeophysics*, Water Sci. Technol. Library Ser., vol. *50*, edited by Y. Rubin and S. S. Hubbard, pp. 185–213, Springer, New York.

Archie, G. E. (1942), The electrical resistivity logs as an aid determining some reservoir characteristics, *Trans. AIME*, *146*, 54–61.

Baú, D., and A. S. Mayer (2008), Optimal design of pump-and-treat systems under uncertain hydraulic conductivity and plume distribution, *J. Contam. Hydrol.*, *100*, 30–46, doi:10.1016/j.jconhyd.2008.05.002.

Binley, A., and A. Kemna (2005), DC resistivity and induced polarization methods, in *Hydrogeophysics*, Water Sci. Technol. Library Ser., vol. *50*, edited by Y. Rubin and S. S. Hubbard, pp. 129–156, Springer, New York.

Binley, A., G. Cassiani, R. Middleton, and P. Winship (2002), Vadose zone flow model parametrisation using cross-borehole radar and resistivity imaging, *J. Hydrol.*, *267*, 147–159.

Brovelli, A., and G. Cassiani (2010), A combination of the Hashin-Shtrikman bounds aimed at modelling electrical conductivity and permittivity of variably saturated porous media, *Geoph. J. Int.*, *180*, 225–237, doi:10.1111/j.1365-246X.2009.04415.x.

Brovelli, A., and G. Cassiani (2011), Combined estimation of effective electrical conductivity and permittivity for soil monitoring, *Water Resour. Res.*, *47*, W08510, doi:10.1029/2011WR010487.

Cassiani, G., V. Bruno, A. Villa, N. Fusi, and A. Binley (2006), A saline tracer test monitored via time-lapse surface electrical resistivity tomography, *J. Appl. Geophys.*, *59*, 244–259.

Castagna, M., and A. Bellin (2009), A Bayesian approach for inversion of hydraulic tomographic data, *Water Resour. Res.*, *45*(4), W04410, doi:10.1029/2008WR007078.

Chen, Y., and D. Zhang (2006), Data assimilation for transient flow in geologic formations via ensemble Kalman filter, *Adv. Water Resour.*, *29*, 1107–1122.

Coscia, I., S. A. Greenhalgh, N. Linde, J. Doetsch, L. Marescot, T. Gunther, T. Vogt, and A. G. Green (2011), 3D crosshole ERT for aquifer characterization and monitoring of infiltrating river water, *Geophysics*, *76*(2), G49–G59, doi:10.1190/1.3553003.

Crestani, E., M. Camporese, and P. Salandin (2010), Hydraulic conductivity assessment via tracer test data assimilation: A comparison of updating techniques, Proceedings of the 4th IAHR International Groundwater Symposium, Valencia, 22–24 September 2010, paper no. 54, 16 pp.

Dagan, G. (1987), Theory of solute transport by groundwater, *Ann. Rev. Fluid Mech.*, *19*, 183–215.

Dagan, G. (1989), *Flow and Transport in Porous Formations*, Springer, New York.

Daily, W. D., A. L. Ramirez, D. J. LaBrecque, and J. Nitao (1992), Electrical resistivity tomography of vadose water movement, *Water Resour. Res.*, *28*, 1429–1442.

Deiana, R., G. Cassiani, A. Kemna, A. Villa, V. Bruno, and A. Bagliani (2007), An experiment of non invasive characterization of the vadose zone via water injection and cross-hole time-lapse geophysical monitoring, *Near Surf. Geophys.*, *5*, 183–194.

Deiana, R., G. Cassiani, A. Villa, A. Bagliani, and V. Bruno (2008), Model calibration of a water injection test in the vadose zone of the Po River plain using GPR cross-hole data, *Vadose Zone J.*, *7*, 215–226, doi:10.2136/vzj2006.0137.

Deutsch, C. V., and A. G. Journel (1997), *GSLIB: Geostatistical Software Library and User's Guide*, 2nd ed., Oxford University Press, Oxford.

Evensen, G. (1994), Sequential data assimilation with a nonlinear quasi-geostrophic model using Monte Carlo methods to forecast error statistics, *J. Geophys. Res.*, *99*(C5), 10,143–10,162.

Evensen, G. (2003), The ensemble Kalman filter: theoretical formulation and practical implementation, *Ocean Dyn.*, *53*, 343–367.

Evensen, G. (2004), Sampling strategies and square root analysis schemes for the EnKF, *Ocean Dyn.*, *54*, 539–560.

Evensen, G. (2006), *Data Assimilation: The Ensemble Kalman Filter*, Springer, New York.

Evensen, G. (2009), The ensemble Kalman filter for combined state and parameter estimation, *IEEE Contr. Syst. Mag.*, *29*(3), 83–104, doi:10.1109/MCS.2009.932223.

Ferré, T., L. Bentley, A. Binley, N. Linde, A. Kemna, K. Singha, K. Holliger, J. Huisman, and B. Minsley (2009), Critical steps for the continuing advancement of hydrogeophysics, *Eos Trans. AGU*, *90*(23), doi:10.1029/2009EO230004.

Finsterle, S., and M. B. Kowalsky (2008), Joint hydrological-geophysical inversion for soil structure identification, *Vadose Zone J.*, *7*, 287–293, doi:10.2136/vzj2006.0078.

Gelhar, L. W. (1993), *Stochastic Subsurface Hydrology*, Prentice-Hall, Englewood Cliffs, NJ.

Hendricks Franssen, H. J., and W. Kinzelbach (2008), Real-time groundwater flow modeling with the Ensemble Kalman Filter: Joint estimation of states and parameters and the filter inbreeding problem, *Water Resour. Res.*, *44*, W09408, doi:10.1029/2007WR006505.

Hinnell, A. C., T. P. A. Ferré, J. A. Vrugt, J. A. Huisman, S. Moysey, J. R ings, and M. B. Kowalsky (2010), Improved extraction of hydrologic information from geophysical data through coupled hydrogeophysical inversion, *Water Resour. Res.*, *46*, W00D40, doi:10.1029/2008WR007060.

Huisman, J. A., J. Rings, J. A. Vrugt, J. Sorg, and H. Vereecken (2010), Hydraulic properties of a model dike from coupled Bayesian and multi-criteria hydrogeophysical inversion, *J. Hydrol.*, *380*(1–2), 62–73, doi:10.1016/j.jhydrol.2009.10.023.

Irving, J., and K. Singha (2010), Stochastic inversion of tracer test and electrical geophysical data to estimate hydraulic conductivities, *Water Resour. Res.*, *46*(11), W11514, doi:10.1029/2009WR008340.

Jadoon, K. Z., E. Slob, M. Vanclooster, and H. Vereecken (2008), Uniqueness and stability analysis of hydrogeophysical inversion for time-lapse ground-penetrating radar estimates of shallow soil hydraulic properties, *Water Resour. Res.*, *44*, W09421, doi:10.1029/2007WR006639.

Kalman, R. E. (1960), A new approach to linear filtering and prediction problems, *J. Basic Eng.*, *82*, 35–45.

Kemna, A., J. Vanderborght, B. Kulessa, and H. Vereecken (2002), Imaging and characterisation of subsurface solute transport using electrical resistivity tomography (ERT) and equivalent transport models, *J. Hydrol.*, *267*, 125–146.

Kowalsky, M. B., S. Finsterle, J. Peterson, S. Hubbard, Y. Rubin, E. Majer, A. Ward, and G. Gee (2005), Estimation of field-scale soil hydraulic and dielectric parameters through joint inversion of GPR and hydrological data, *Water Resour. Res.*, *41*, W11425, doi:10.1029/2005WR004237.

LeBlanc, D. R., S. P. Garabedian, K. M. Hess, L. W. Gelhar, R. D. Quadri, K. G. Stollenwerk, and W. W. Wood (1991), Large-scale natural gradient tracer test in sand and gravel, Cape-Cod, Massachusetts. 1. Experimental-design and observed tracer movement, *Water Resour. Res.*, *27*(5), 895–910.

Lehikoinen, A., J. M. J. Huttunen, S. Finsterle, M. B. Kowalsky, and J. P. Kaipio (2010), Dynamic inversion for hydrological process monitoring with electrical resistance tomography under model uncertainties, *Water Resour. Res.*, *46*, W04513, doi:10.1029/2009WR008470.

Liu, G. S., Y. Chen, and D. X. Zhang (2008), Investigation of flow and transport processes at the MADE site using ensemble Kalman filter, *Adv. Water Resour.*, *31*(7), 975–986, doi:10.1016/j.advwatres.2008.03.006.

Looms, M. C., A. Binley, K. H. Jensen, L. Nielsen, and T. M. Hansen (2007), Identifying unsaturated hydraulic parameters using an integrated data fusion approach on cross-borehole geophysical data, *Vadose Zone J.*, *7*, 238–248.

Margulis, S. A., D. McLaughlin, D. Entekhabi, and S. Dunne (2002), Land data assimilation and estimation of soil moisture using measurements from the Southern Great Plains 1997 Field Experiment, *Water Resour. Res.*, *38*(12), 1299, doi:10.1029/2001WR001114.

Menke, W. (1984), *Geophysical Data Analysis: Discrete Inverse Theory*, Academic, New York.

Monego, M., G. Cassiani, R. Deiana, M. Putti, G. Passadore, and L. Altissimo (2010), Tracer test in a shallow heterogeneous aquifer monitored via time-lapse surface ERT, *Geophysics*, *75*(4), WA61–WA73, doi:10.1190/1.3474601.

Neuman, S. P., A. Blattstein, M. Riva, D. M. Tartakovsky, A. Guadagnini, and T. Ptak (2007), Type curve interpretation of late-time pumping test data in randomly heterogeneous aquifers, *Water Resour. Res.*, *43*(10), W10421, doi:10.1029/2007WR005871.

Pollock, D., and O. A. Cirpka (2010), Fully coupled hydrogeophysical inversion of synthetic salt tracer experiments, *Water Resour. Res.*, *46*, W07501, doi:10.1029/2009WR008575.

Pollock, D. W. (1988), Semianalytical computation of path lines for finite-difference models, *Ground Water*, *26*(6), 743–750.

Rings, J., J. A. Huisman, and H. Vereecken (2010), Coupled hydrogeophysical parameter estimation using a sequential Bayesian approach, *Hydrol. Earth Syst. Sci.*, *14*, 545–556.

Rubin, Y. (2003), *Applied Stochastic Hydrogeology*, Oxford University Press, Oxford.

Rubin, Y., and S. S. Hubbard, Eds. (2005), *Hydrogeophysics*, Springer, Dordrecht, Netherlands.

Salandin, P., V. Fiorotto, and L. Da Deppo (2000), Particle's tracking in 3-D heterogeneous porous media transport models, in *Computational Methods, Surface Water System and Hydrology*, edited by Bentley et al., pp. 813–818, Balkema, Rotterdam, Netherlands.

Sambuelli, L., and C. Comina (2010), Fast ERT to estimate pollutants and solid transport variation in water flow: A laboratory experiment, *Boll. Geof. Teor. Appl.*, *51*(1), 1–22.

Singha, K., and S. M. Gorelick (2005), Saline tracer visualized with three-dimensional electrical resistivity tomography: Field-scale spatial moment analysis, *Water Resour. Res.*, *41*, W05023, doi:10.1029/2004WR003460.

Sudicky, E. A. (1986), A natural gradient experiment on solute transport in a sand aquifer—Spatial variability of hydraulic conductivity and its role in the dispersion process, *Water Resour. Res.*, *22*(13), 2069–2082.

Sudicky, E. A., W. A. Illman, I. K. Goltz, J. J. Adams, and R. G. Mclaren (2010), Heterogeneity in hydraulic conductivity and its role on the macroscale transport of a solute plume: From measurements to a practical application of stochastic flow and transport theory, *Water Resour. Res.*, *46*, W01508, doi:10.1029/2008WR007558.

Tikhonov, A. N., and V. Y. Arsenin (1977), *Solutions of Ill-Posed Problems*, W. H. Winston and Sons, Winston, Washington D.C.

Vanderborght, J., A. Kemna, H. Hardelauf, and H. Vereecken (2005), Potential of electrical resistivity tomography to infer aquifer transport characteristics from tracer studies: A synthetic case study, *Water Resour. Res.*, *41*, W06013, doi:10.1029/2004WR003774.

Vereecken, H., A. Binley, G. Cassiani, I. Kharkhordin, A. Revil, and K. Titov (2006) *Applied Hydrogeophysics*, Springer, Berlin.

Zhang, D. (2002), *Stochastic Methods for Flow in Porous Media: Coping With Uncertainties*, Academic, San Diego.

M. Camporese and P. Salandin, Dipartimento di Ingegneria Idraulica, Marittima, Ambientale e Geotecnica, Università degli Studi di Padova, Via Loredan 20, I-35131, Padova, Italy. (camporese@idra.unipd.it; sala@idra.unipd.it)

G. Cassiani and R. Deiana, Dipartimento di Geoscienze, Università degli Studi di Padova, Via Gradenigo 6, I-35131, Padova, Italy. (giorgio.cassiani@unipd.it; rita.deiana@unipd.it)